Influence of Z-Pin Size and Density on the Compressive Response of Woven Glass Fiber Composites

Hsengji Huang, Anthony M. Waas
Department of Aerospace Engineering
University of Michigan, Ann Arbor, MI, 48109-2140, USA
Keywords: *Z-pins, woven composites, kink band, crack*

Abstract

Experimental results pertaining to the compressive response of Z-pinned S-Glass fiber plain weave composites are presented. These experiments are motivated by a need to know the effect of Z-pinning on the strength and stiffness of these composites. A series of experiments are performed based upon density of the Z-pins and the diameter of the Z-pins. It is concluded that the damage zone around a Z-pin plays an important role in influencing the stiffness and strength of the Z-pin composite. 2D and 3D finite element (FE) based numerical models (based upon the composite microstructure acquired from scanning electron micrograph-SEM images) are used to capture details of the observed failure mechanisms and to provide predictions of the stiffness and strength of the composite.

1 Introduction

Delamination resistance of layered textile composites can be improved by Z-pinning. Evidence of such improvements are discussed in [1], [2], and [3]. While improvement in out of plane resistance is desired, a simultaneous degradation (or improvement) in in-plane response remains to be systematically explored. In this paper, results for the in-plane compression response of Z-pinned S2-Glass fiber plain weave composites are presented. For a fixed Z-pin diameter, the effect of Z-pin density is examined for 2 different Z-pin diameters. Two types of stacking are examined. One is a quasi-isotropic lay-up, while the other is a cross-ply lay-up borrowing from the terminology for laminated straight fiber reinforced composites. The failure mechanism in all cases is kink banding within the axial tows, which can be found in all of the failed specimens. Based upon SEM images of the composite microstricture, appropriate 2D and 3D FE models are used for predictions.

2 Compressive Tests

Plain weave S2 Glass fabrics are sized, Z-pinned and infused with epoxy resin to make tow types of laminated textile composites. The glass fiber tows contain 9k fibers with a nominal fiber volume fraction of 52%. Measurements indicate a mean major tow diameter of 4.4 mm and a mean minor tow diameter of 0.4 mm in the cured state. The Z-pins are two types. The larger diameter is a T650 carbon fiber in a BMI matrix, while the smaller diameter is a T300 carbon fiber in a BMI matrix . The fiber volume fraction of the Z-pins is 64 %. The stacked 16 layer laminates are 12 mm thick. Specimens are categorized into 6 groups. Group A, group C, and group E are [45/-45/0/90]2S lay-ups, with Z-pin diameters of 0.5080 mm (0.02 in.), 0.2794 mm (0.011 in.), and no Z-pin, respectively. Group B, group D, and group F are [0]16 lay-ups with Z-pin diameter of 0.5080 mm (0.02 in.), 0.2794 mm (0.011 in.), and no Z-pin, respectively. It is to be noted that group A, group C, and group E are quasi-isotropic composites while group B, group D, and group F are cross-ply composites. From group A to group D, each group is further sub-divided into three subgroups based on the Z-pin density (1%, 2%, or 3%). Detailed descriptions of these 6 groups are given in Table1.

Table 1

Type	Description	Size
A-1	UAZ-T6B-0.020”-1%	38.1cm x 38.1cm
A-2	UAZ-T6B-0.020”-2%	38.1cm x 38.1cm
A-3	UAZ-T6B-0.020”-3%	38.1cm x 38.1cm
B-1	UAZ-T6B-0.020”-1%	38.1cm x 38.1cm
B-2	UAZ-T6B-0.020”-2%	38.1cm x 38.1cm
B-3	UAZ-T6B-0.020”-3%	38.1cm x 38.1cm
C-1	UAZ-T3B-0.011”-1%	38.1cm x 38.1cm
C-2	UAZ-T3B-0.011”-2%	38.1cm x 38.1cm
C-3	UAZ-T3B-0.011”-3%	38.1cm x 38.1cm
D-1	UAZ-T3B-0.011”-1%	38.1cm x 38.1cm
D-2	UAZ-T3B-0.011”-2%	38.1cm x 38.1cm
D-3	UAZ-T3B-0.011”-3%	38.1cm x 38.1cm
E	No Z-Pins	38.1cm x 38.1cm
F	No Z-Pins	38.1cm x 38.1cm

2.1 Compressive Loading Apparatus

Compressive tests were performed on a servo-hydraulic MTS machine with a displacement control loading rate of 0.010 mm/sec. An image of the experimental setup is shown in Figure 1. In order to obtain the compressive strength of the material, the specimen is prevented from global buckling by using anti-buckling guides (knife edge supports that allow in-plane sliding and out-of-plane rotation, but constraints out-of-plane deflection) as indicated in a top-view image of the support fixture shown in Figure 2. The front view and back view of a typical specimen is shown in Figure 3. The width of the specimen is 63.5 mm (2.5 in.) and the height of the specimen is 50.8 mm (2 in.). For each experiment, two strain gages were attached to the specimen (back to back) aligned with the loading direction and one in the transverse direction on one side. The purpose of using two strain gages in the loading direction is to monitor any unwanted bending that may occur during the compression loading.

2.2 Compressive Stiffness

Figure 4 shows a comparison of the slope of the axial stress (defined as load divided by nominal cross-sectional area) - axial strain (averaged between the two back to back axial strain gages) curves, between group A and group E. This measure corresponds to the axial Young's modulus of the specimen. Figure 5 shows a comparison of the Young's moduli between group B and group F. The horizontal axis represents density of the Z-pins and the vertical axis represents the corresponding Young's modulus. Figure 6 and Figure 7 show the comparison of group C and group D with the corresponding no Z-pin composites group. For group A and C, the Young's modulus decreases as the density of the Z-pins increases. However, the decrease of the Young's modulus is not significant. This is consistent with the conclusion in [4] that the Young's modulus decreases 7% to 10% by adding 2% density of Z-pins. In other work described in [5], [6], and [7], it is shown that the Young's modulus has a trend to degrade with the increase of Z-pin density and the value of Young's modulus doesn't change appreciably when the density of Z-pins is less than 1.5%. However, the Young's modulus can degrade by as much as 30% when the density of Z-pins is in excess of 10% [8]. Comparing Figure 4 with Figure 6 for the subgroup of the same density of Z-pins, say 1%, we can observe that the Young's modulus in group A is slightly higher than that in group C. This can be understood as follows: After insertion of the Z-pins, the Z-pins in subgroup C have a larger contacting area with the surrounding glass fiber tows in the composite than the corresponding contacting area in subgroup A. A larger contacting area leads to a larger probability of the presence of initial interfacial cracks (the Z-pin/matrix boundary acts as a stress raiser) as well as a larger probability of unintended tow undulations, thus inducing stress and strain concentration and a resulting lowering of the axial stiffness. Furthermore, the undulations lead to lowering of the compression strength caused by fiber tow kinking. A further explanation is as follows: for composites with the same Z-pin density, each Z-pin of diameter 0.508 mm (0.02 in.) inserted in the composites can be "replaced" by four Z-pins of diameter 0.254 mm (0.01 in.) Z-pins as shown in Figure 8. Suppose that the height of the composites is h. Then, the contacting area in the through-the thickness direction around one Z-pin of diameter d=0.508 mm (0.02 in.) is $0.508\pi h$. The contacting area around the four smaller (d=0.2540 mm) Z-pins is $1.016\pi h$. This shows that the smaller diameter Z-pin has a larger "contacting area" than a Z-pin with d=0.5080 mm (0.02 in.) provided that the density of the Z-pins is the same. Under this circumstance, it is likely that, in the composites of d=0.254 mm (0.01 in.), more damage is probable during the insertion of the Z-pins. Figure 9 shows scanning electron microscope (SEM) images of a d=0.508 mm (0.02 in.) Z-pin composite and a d=0.2794 mm (0.011 in.) Z-pin composite, respectively. Both of these images were taken from as manufactured plaques prior to conducting compression experiments. The monitored image plane (xy) is cut at the center of the thickness as shown in Figure 9. These images show that Z-pin insertion and subsequent cure leads to interfacial damage and an interfacial crack can be seen at the circumferential boundary of the Z-pin. Therefore, in a given area, as the number of Z-pins increase, the resulting "initial damage" is also larger. This can also explain why a 3% Z-pin composite has slightly lower Young's modulus than the 1% or 2% Z-pin composite.

2.3 Compressive Strength

Figure 10 shows the comparison of the compressive strength between group A and group E. The horizontal axis represents the density of the Z-pins and vertical axis represents the compressive strength. Figure 11 shows the comparison of the compressive strength between group B and group F. Figure 12 shows the comparison of the compressive

strength between group C and group E. Finally, Figure 13 shows the comparison of the compressive strength between group D and group F. From Figure 10 to Figure 13, it is observed that the compressive strength decreases as the density of Z-pins increase. For the $[45/-45/0/90]_{2S}$ composites of group A and group C, the subgroups of the composites with the same Z-pin density are compared. It is found that the strength of the subgroup in group A is higher than that of the subgroup in group C. The same trend is also observed for the comparison of group B and group D, which show that subgroups in group B are higher in compression strength than those in group D when the same density is specified. The reason that the strengths in group A is lager than group C and that group B are higher than group D is as follows: The Z-pins in subgroups C and D have more contacting area with the glass fiber tows than that in subgroups A and B. Therefore, these subgroups contain a larger population of initial "defects" leading to a lowering of the compression strength. The role of these sites (which are within axial tows) in initiating fiber kink banding within the axial tows are discussed later.

2.4 Compression Failure Mechanism

Figure 14 shows an image of the failure pattern that is typical for most of the Z-pin composites under compression. It is noticed that all failed specimens exhibit the same pattern. That is, an out of plane macroscopic kink band can be found. Further examination with SEM images shows that individual fiber tows kink due to unintended initial fiber misalignment caused by Z-pin insertion. Figure 15 shows the crack path passing through the area around Z-pins. These sites are location of stress (strain) concentration. It is also observed, in Figure 16, that a kink band formed between the two Z-pins within one specimen of group C1. Figure 17 shows existence of kind band and cracks around the Z-pins of the specimen in group A2 and group A3, respectively. These failure mechanisms are repeatedly found in all of the specimens.

The typical failure pattern for composites without Z-pins is shown in Figure 18. As shown before with the Z-pin composites, an out of plane macroscopic kind band can be found. If we examine the side view in Figure 18, slight lateral expansion is noticed as opposed to the side view in Figure 14. This is because the Z-pins provide constraint in the through the thickness direction. Previous work has found that this through-the-thickness constraint is responsible for an increase in the interlaminar fracture toughness [1,2,3].

3 Numerical Simulation

3.1 Creation of finite element model

In order to build the three dimensional model to perform finite element analysis, the geometry of representative unit cell has to be identified first. The traditional textile composites are composed of the fiber tows and matrix as shown in Figure 19. For the Z-pin textile composites, Z-pins are inserted through the thickness in the composites. As shown in Figure 20, the fiber tow is an undulating, nearly sinusoidal, solid entity in a 3D setting. Therefore, the sinusoidal shape of the fiber tow is assumed in this 3 D model. The cross section of the fiber tow is assumed to have elliptic shape, based on SEM images of the cured composite. The geometry of the sinusoidal tow and the cross section of the tow used in the simulation is estimated through statistics of 40 similar images to Figure 21. The average geometry is used in the FE model. The average amplitude of the sinusoidal tow, the major axis, and minor axis are indicated in Figure 22. In the representative unit cell (RUC), two longitudinal and two transverse sinusoidal fiber twos are simulated as shown in Figure 23. Two tows in each direction (longitudinal or transverse) have the same geometry and the two tows in each direction differ in phase angle.

It is to be noted that only one layer of $[0]_{16}$ composites is constructed and used in the finite element simulation. These longitudinal and transverse fiber tows are embedded in the matrix shown in Figure 24. The Z-pin fibers are embedded in the matrix and fiber tows.

After the geometry is identified, the constitutive law of each constituent is needed in order to implement the finite element model in the context of a nonlinear (material and geometry) analysis. The response curve of the in-situ matrix is first extracted by carrying out experiments on the cured composite as described in [9]. The extracted response curve of the in-situ matrix (axial stress – axial strain) as shown in Figure 25 is obtained, it is used to obtain the response curves of the three dimensional fiber tow. The fiber tow consists of matrix and fiber filaments as shown in Figure 26. Therefore, the property of the matrix will influence the property of the fiber tow, most importantly the transverse properties. Forty images similar to Figure 26 are taken to estimate the fiber volume fraction of the tows. The fiber volume fraction and matrix volume fraction in a fiber tow are 52% and 48%,

respectively. These numbers are used to build a hexagonal representative unit cell of the tow. A three dimensional hexagonal representative unit cell shown in Figure 27 is used to obtain the constitutive law of the fiber tow in accordance with a elastic-plastic representation. It is pointed out in [10] that hexagonal representative unit cell provides the requisite symmetries associated with transverse isotropy resulting in estimates that are better than a square representative unit cell. A FE analysis is performed to obtain the constants associated with an orthotropic plastic potential for the fiber tow.

The matrix is assumed to obey a J2 isotropic hardening law in the simulation. A simplified orthotropic plastic potential proposed in [11] is used in this paper,

$$f = \frac{1}{2}[(\sigma_{22} - \sigma_{33})^2 + 2a_{44}\sigma_{23}{}^2 + 2a_{55}\sigma_{21}{}^2 + 2a_{55}\sigma_{31}{}^2] \quad (1)$$

Because of symmetry, only 2 parameters are needed in equation (1). As shown in Figure 27, the direction 1 is the longitudinal direction of the fiber tow. Direction 2 and direction 3 are the transverse directions of the fiber tow. It is to be note that equation 1 is assumed that no plastic deformation occurs in the longitudinal direction of the fiber tow. The yield surface can be obtained from performing a transverse compressive simulation in direction 2(or direction 3). From this simulation, the yield stress σ_{22} or σ_{33} can be identified. The plastic surface corresponding to yielding can be obtained.

$$f_{yield1} = 0.5\sigma_{22}{}^2 \quad (2)$$

Subsequently, a shear simulation in the 12 plane is performed. From the stress-strain curve, the yield stress can be identified. Then, the coefficient a_{55} can be obtained by use of equation 1 because the plastic yield surface has been obtained from compressive simulation in direction 2. That is, equation 2 and equation 3 should be equivalent.

$$f_{yield1} = a_{55}\sigma_{21}{}^2 \quad (3)$$

Similarly, parameter a_{44} can be extracted by performing shear simulation in direction 23.

3.2 2D finite element analysis

A 2D finite element model is built based on the SEM image shown in Figure 28. The purpose of the 2D model is to investigate the difference of the local behavior of fiber tows when the Z-pin is present or when the Z-pin is absent. This 2D model can be used to interrogate the compressive kinking behavior of the tows which is a strength limiting mechanism in compression. The aforementioned material properties obtained in section 3.1 are specialized to 2D and used in the 2D finite element simulation, which incorporates geometric nonlinearity and is carried out under displacement control with a arc-length solver [see, [12] for a similar analysis]. Figure 29 shows the comparison of the response for different diameters of the composites when the 1% density of Z-pins are inserted in the composites. The d=0.508 mm (0.02 in) composites have a lower strength than d=0.2794 mm (0.011 in) one. The deformed shape of the d=0.508 mm (0.02 in) composites at the peak load and post failure state are both presented. The kink band which emerges just prior to attainment of the peak strength can be observed in the post failure contour plot. Notice the highly localized bands where there is large inelastic action. Figure 30 shows a comparison between different density (1% and 2%) corresponding to d=0.508 mm (0.02 in) Z-pins. The 2% composites have a lower strength than the 1% composites. It is seen that the composites behave linearly until the attainment of kinking which is caused by the reduced stiffness in the transverse direction which is responsible for precipitating a kink band.

As observed in Figure 28, cracks can always be found near the contacting surface between matrix and Z-pin. That shows that the contacting area is not perfectly bonding between matrix and Z-pins. Therefore, the assumption of perfect bonding between the matrix and Z-pin may not be accurate. Here, an extreme damage case can be modeled by assuming that the Z-pin is completely absent. The comparison of this “damage” case (with a hole, no Z-pin) and the “non damage” case is shown in Figure 30. It is observed that damage between matrix and Z-pin doesn’t influence the strength of the composites. However, it has a strong influence on the post failure behavior. The analysis results from the 2D model are useful for understanding the observed experimental trends in failure initiation by kink banding, while at the same time they serve as input for the 3D modeling.

3.3 3D finite element analysis

Figure 33, Figure 34, and Figure 35 show the fiber tows of a 3D model of composites with no Z-pin, 1%, d=0.5080 mm (0.02 in.) Z-pin, and 1% d=0.2794 mm (0.011 in.) Z-pin. During the simulation, displacement is imposed in the global “1” - direction. In addition, an arc-length solver is used in conjunction with geometric non-linearity. The tows are modeled as described earlier in section 3.1 The results of simulations are shown in Figure

36. It is observed that the strength of composites without Z-pins is higher than those with Z-pins. Furthermore, d=0.2794 mm (0.011 in.) Z-pin composites have a lower strength than the d=0.5080 mm (0.02 in.) composites. This is consistent with what is found in the experiments. The experimental result in Figure 36 corresponds to a compressive response without Z-pins. It is noted that the predicted compressive response is in close agreement with that obtained from experiments. The deformed fiber tows of the composites (with no Z-pins) at the peak load and the post failure state are also illustrated in Figure 36.

4 Conclusions

Initial defects between the Z-pin and the surrounding area and unintended fiber waviness caused by Z-pin insertion have been identified as causes responsible for lowering the compression strength which is limited by tow kinking leading to macroscopic kink banding. When the diameter is set to be the same, the higher density Z-pin composites have lower strength than the lower density Z-pin composite. The higher stress concentration on the higher density composite is shown in section 2. When the density is set to be the same, the small diameter Z-pin composites have lower strength than the larger diameter Z-pin composites. Finally, the numerical methods outlined proves to be a reliable predictor of the compressive strength of the Z-pin composites.

Acknowledgments

HJH and AMW are grateful for the financial sponsorship of the Army Research Office (Bruce LaMattina and Chris Hoppel) and the Department of Aerospace Engineering, University of Michigan. The authors acknowledge that this research is supported, in whole or in part, by Army Research Office cooperative agreement no W911NF-05-1-0259. Such support does not constitute an endorsement by the Army Research Office of the views expressed herein. The Z-pinning by Aztex corporation (Tom Fusco) and the material manufacturing by Bazle Gama (Delaware Composites Center) and Seth Ghiorse (Army Research Labs) are gratefully acknowledged.

References

[1] Robison, P., Das, S. “Mode I DCB testing of composite laminates reinforced with z direction pins: a simple model for the investigation of data reduction strategies”. Engineering Fracture Mechanics, Vol. 71, pp 345–364, 2004.

[2] Byrd, Larry, and Birman, Victor, “The estimate of the effect of z-pins on the strain release rate, fracture and fatigue in a composite co-cured z-pinned double cantilever beam”. Composite Structures, Vol. 68 pp 53–63, 2005.

[3] Dai, S., C., Yan, W., Liu, H., Y., Mai, Y., W. “Experimental study on z-pin bridging aw by pullout test”. Composites Science and Technology, Vol. 64, pp 2451–2457, 2004.

[4] Grassi, C., Zhang, X., Meo, M. “Prediction of stiffness and stresses in z-fibre reinforced composite laminates”. Composites: PartA, Vol. 33, pp 1653–1664, 2002.

[5] Freitas, G., Magee, C., Dardzinski, P., Fusco, T. “Fiber insertion process for improved damage tolerance in aircraft laminates”. J. Advanced Mat., Vol. 25, pp 36–43, 1994.

[6] Freitas, G., Magee, C., Boyce, J., Bott, R. “Service tough composite structures using z-fibers process”. Proc. 9th Dod/NASA/FAA Conf. Comp., Lake Tahoe, pages 2657–2665, Nov 1991.

[7] Freitas, G., Fusco, T., Campbell, T., Harris, J.,Rosenberg, R. “Z-fiber technology and products for enhancing composite design”. Proc. of the 83th Meeting of the AGARD SMP on Bolted/Bonded Joints in Polymeric Composites, pages 17–1–17–8, Sep 2-3,1996.

[8] Steeves, C., Fleck, N. Proc. 12th international Conf. Comp. Mat., July 1999.

[9] Ahn, J. H. Failure mechanisms of notched laminated composites under compressive loading at room and elevated temperature. PhD thesis, University of Michigan, 1999.

[10] Hyer, M. W., Waas, A. W. “Micromechanics of linear elastic continuous fiber composites”. T. W. Chou, ed., Comprehensive Composite Materials, Vol. 1, Chapter

[11] Chen, J. L., Sun, C. T. “A plastic potential function suitable for anisotropic fiber composites”. Journal of Composite Materials, Vol. 27(14), pp 1379–1390, 1993.

[12] Quek, S. , Waas M. A., Khaled W. S. ,Venkatesh A. “Compressive response and failure of braided textile composites: Part 2—computations”, International .Journal of Nonlinear Mechanics, Vol. 39(4), pp 649–663, 2004.

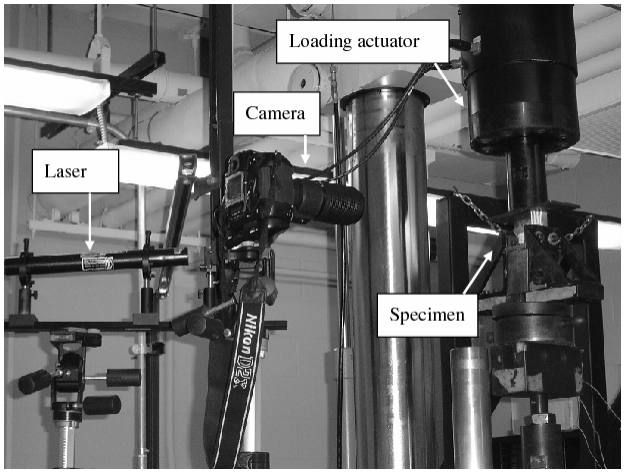

Figure 1 MTS Machine and Speckle Setup

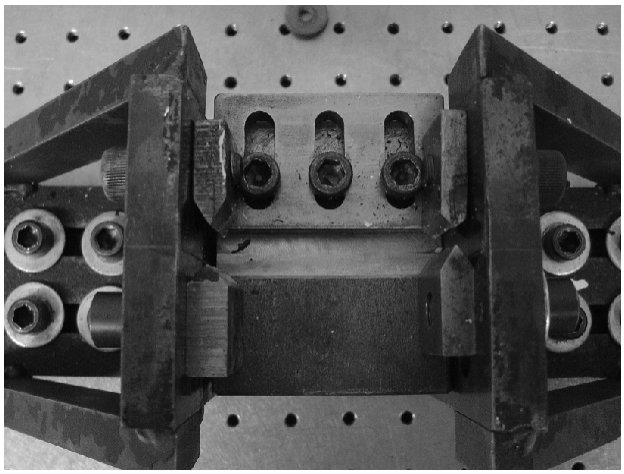

Figure 2 Side Support Fixture

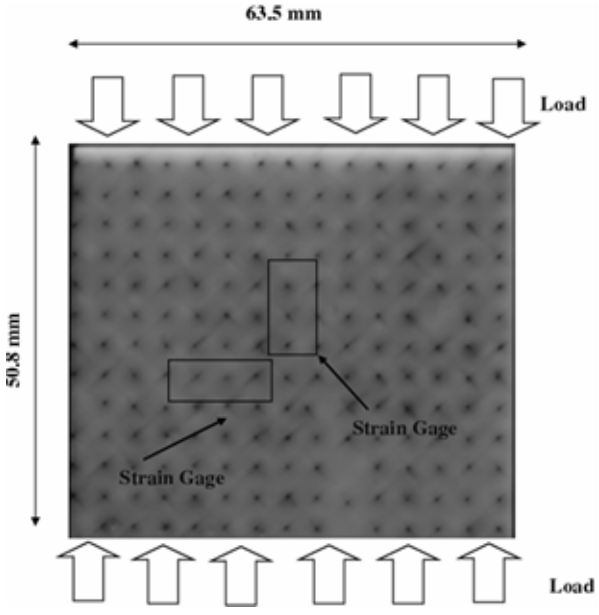

Figure 3 Front View of the Tested Specimen

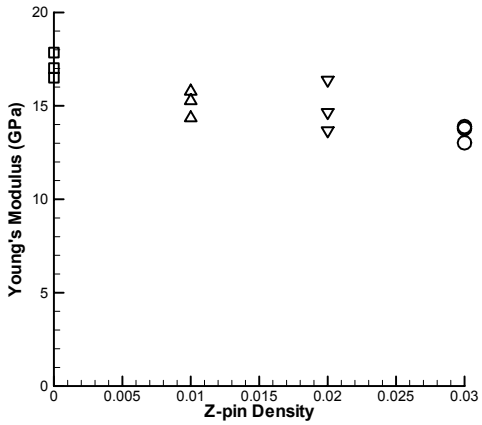

Figure 4 Comparison of Young's Modulus in Group A and Group E

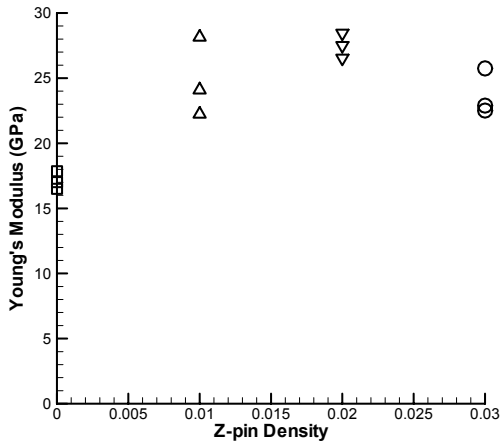

Figure 5 Comparison of Young's Modulus in Group B and Group F

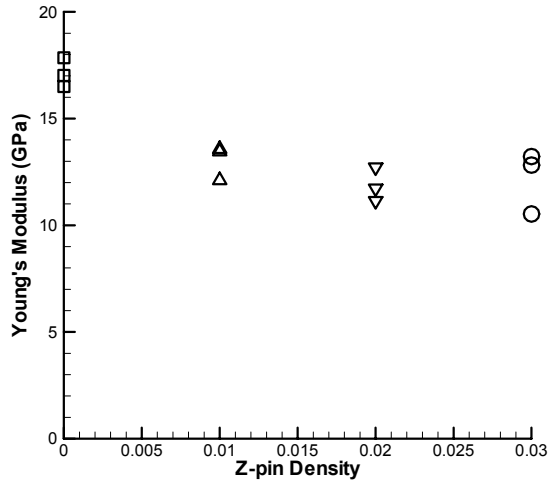

Figure 6 Comparison of Young's Modulus in Group C and Group E

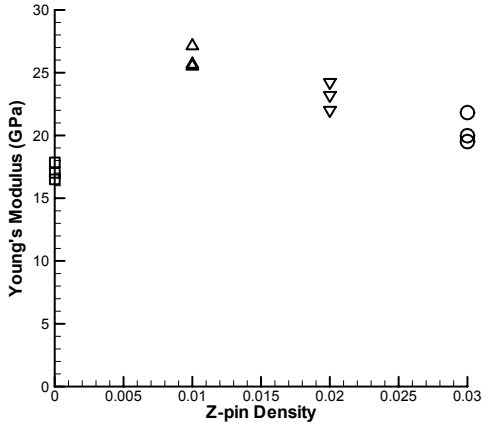

Figure 7 Comparison of Young's Modulus in Group D and Group F

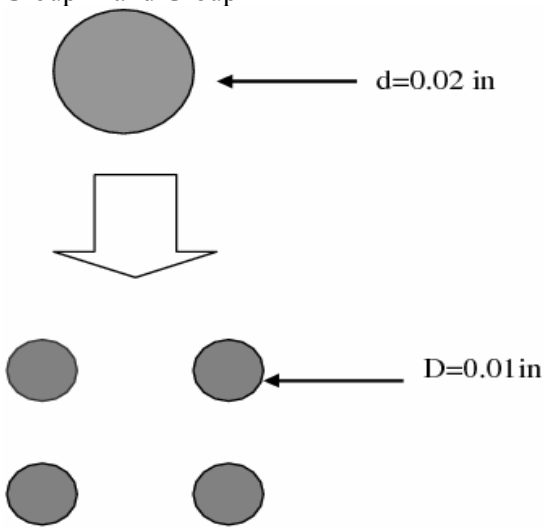

Figure 8 Illustration of d=0.5080 mm (0.02 in.) Z-pin and d=0.2794 mm (0.011 in.) Z-pins

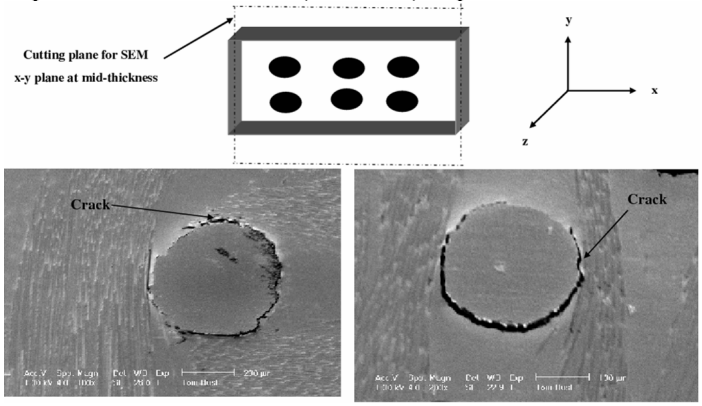

Figure 9 (a) SEM Image of d=0.5080 mm (0.02 in.) Z-pin (b)SEM Image of d=0.2794 mm (0.011 in.) Z-pin

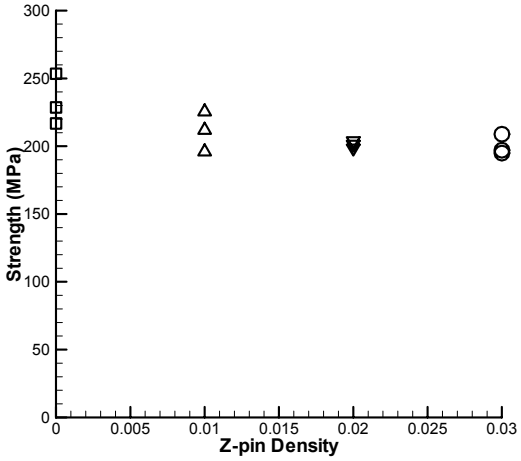

Figure 10 Comparison of the Strength in Group A and Group E

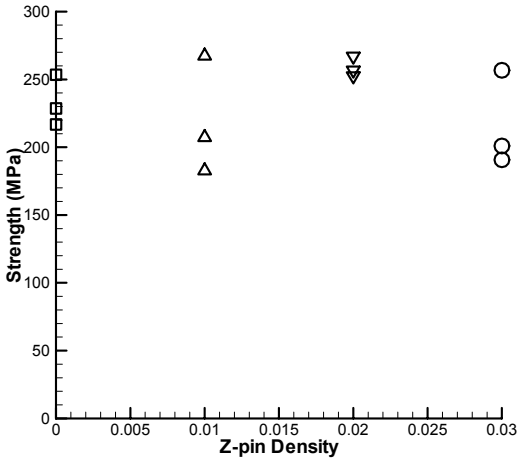

Figure 11 Comparison of the Strength in Group B and Group F

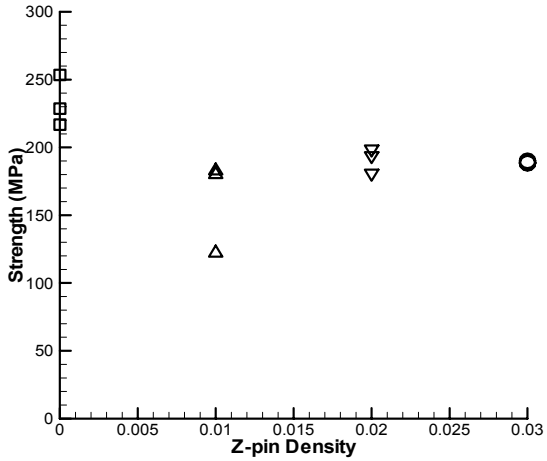

Figure 12 Comparison of the Strength in Group C and Group E

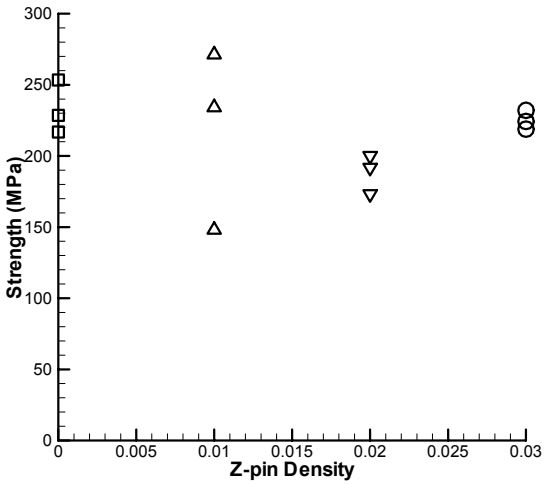

Figure 13 Comparison of the Strength in Group D and Group F

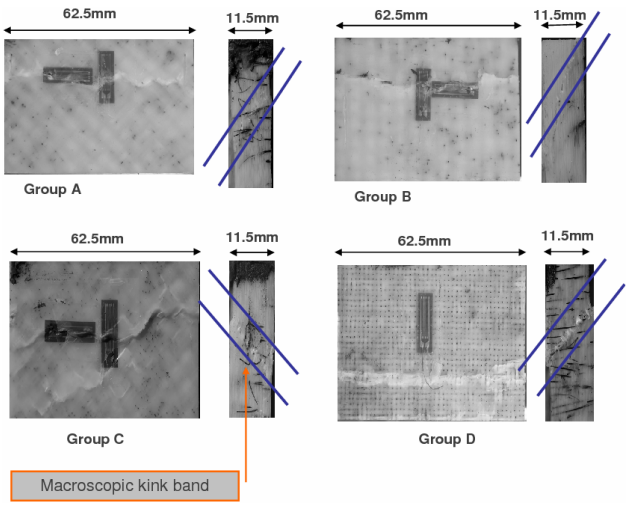

Figure 14 Macroscopic Compression Failure Mechanism for Group A, B, C, and D

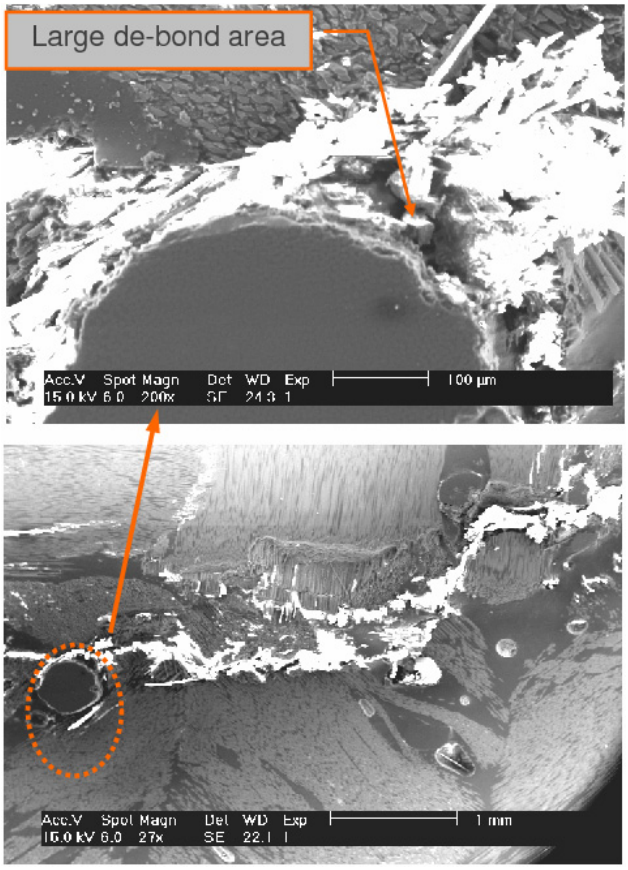

Figure 15 Crack Path in Group A3

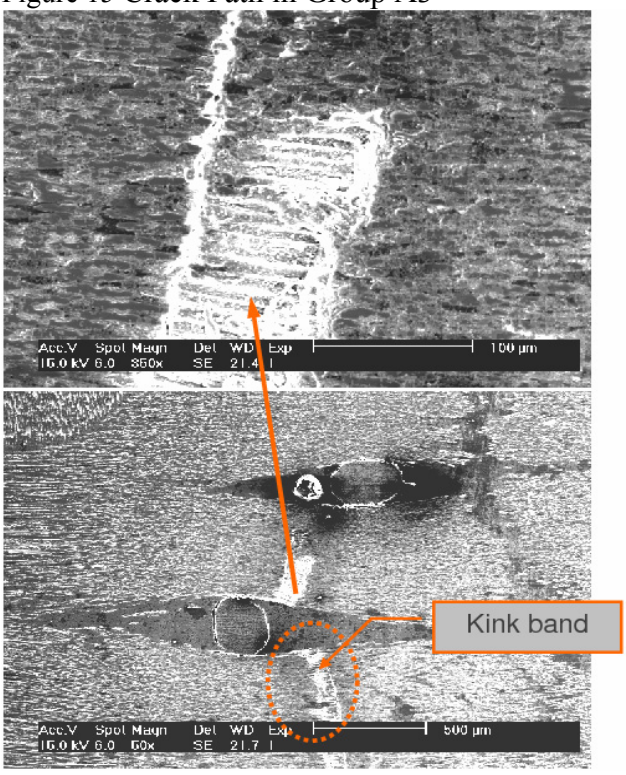

Figure 16 Kink Band in Fiber Tow at the Fiber/Matrix Scale in Group C1

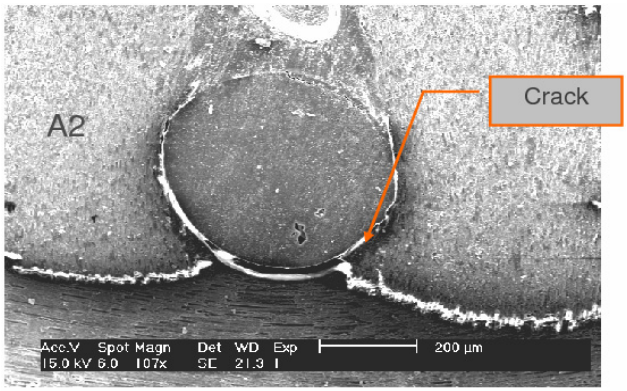

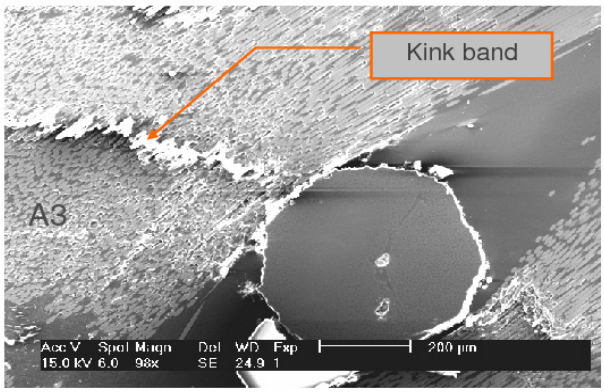

Figure 17 (a) Crack near the Z-pin of Specimen in Group A2 (b) Crack near the Z-pin of Specimen in Group A3

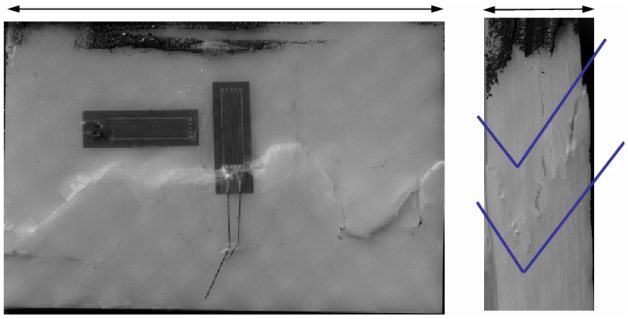

Figure 18 Macroscopic Compression Failure Mechanism for Group E

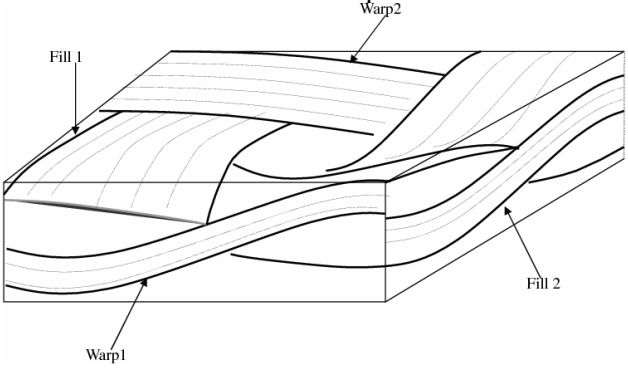

Figure 19 SEM Image of Fiber Tow and Matrix

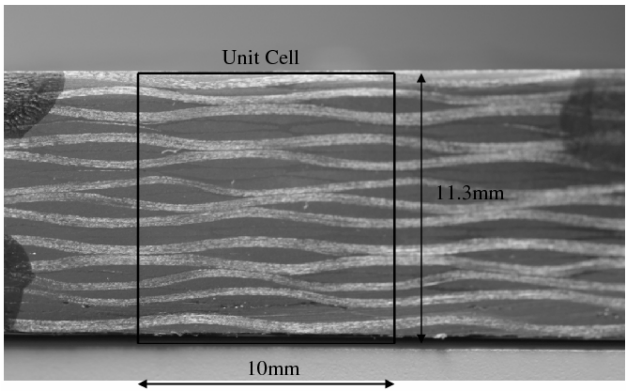

Figure 20 Image of Cross Section

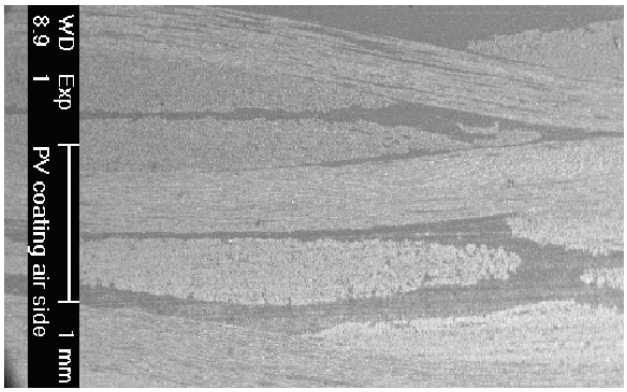

Figure 21 SEM Image of Fiber Tow and Matrix

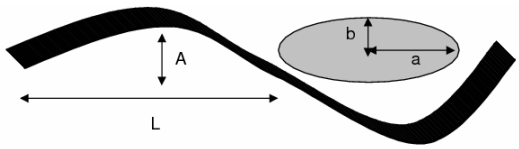

L	A	a	b
5 mm	0.26 mm	2.2 mm	0.2 mm

Figure 22 Fiber Parameters for RUC

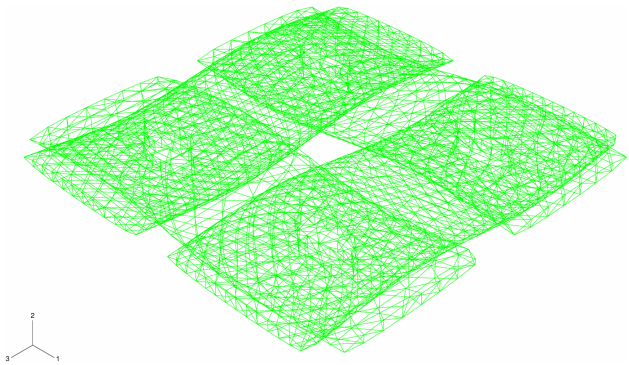

Figure 23 Longitudinal and Transverse Fiber Tows

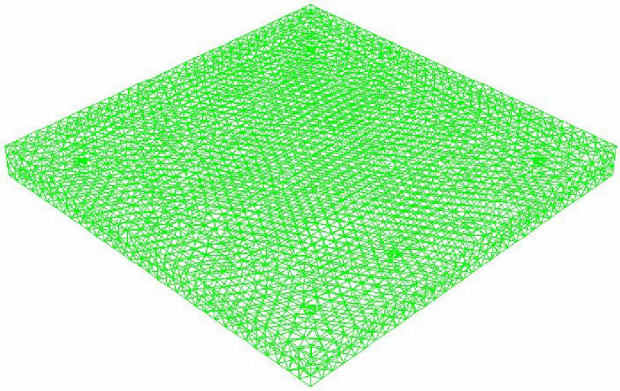

Figure 24 Matrix

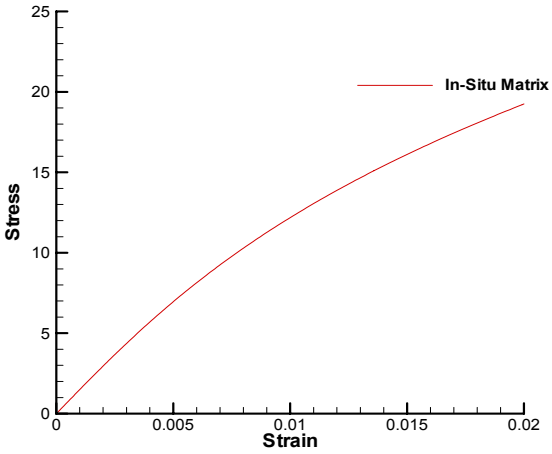

Figure 25 In-Situ Property

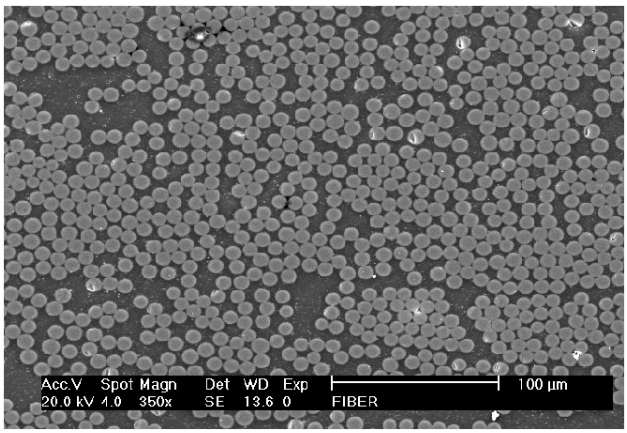

Figure 26 SEM Image within the Fiber Tow

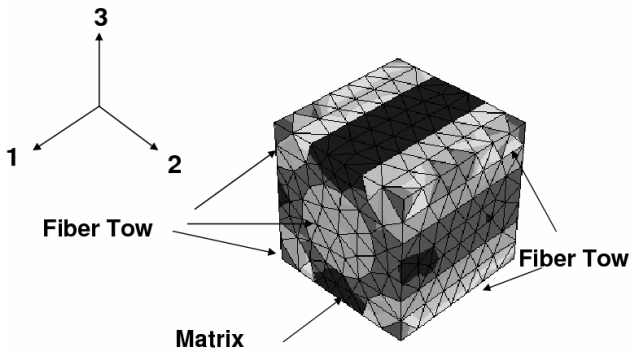

Figure 27 Illustration of the Representative Unit Cell

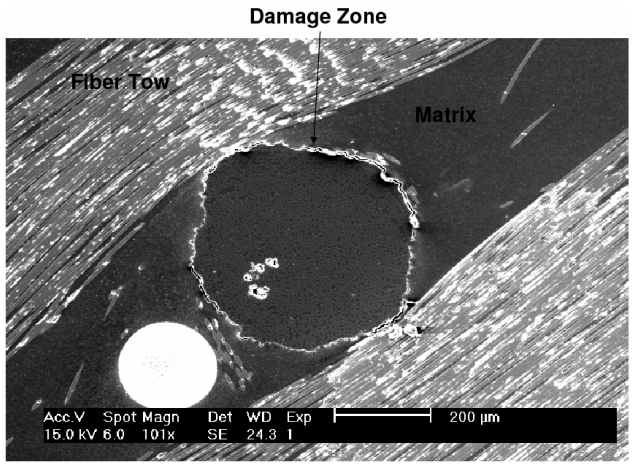

Figure 28 Damage Zone near the Z-pin

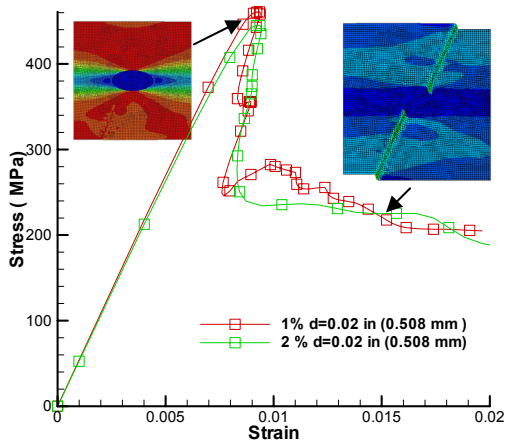

Figure 29 Comparison of Case I and Case III

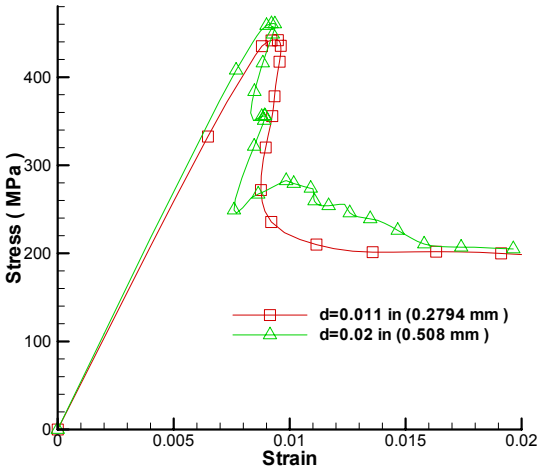

Figure 30 Comparison of Case I and Case II

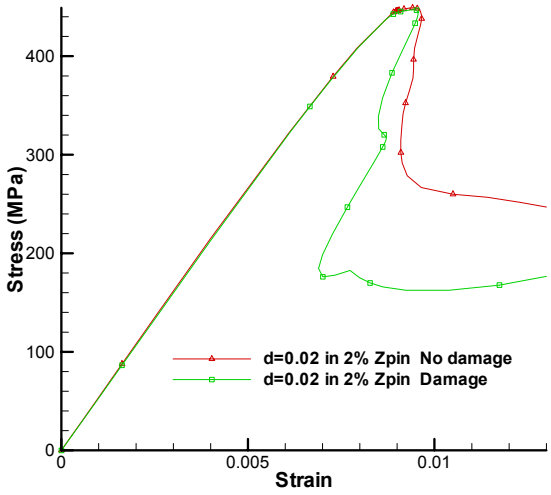

Figure 32 Comparison of Damage Case and non Damage Case

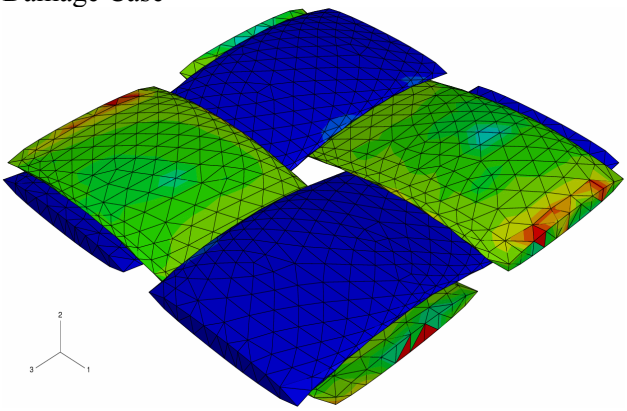

Figure 33 One Unit Cell with no Z-pin

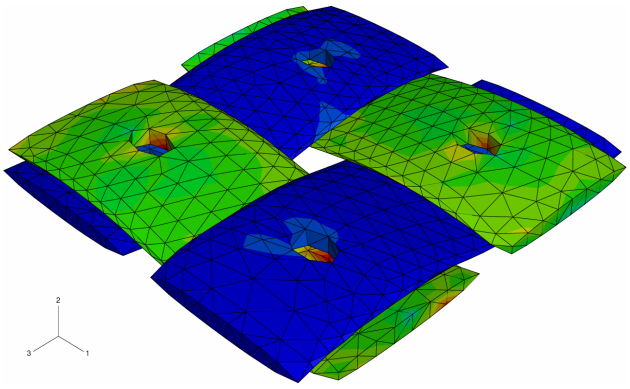

Figure 34 One Unit Cell with 1% d= 0.508 mm (0.02 in) Z-pin

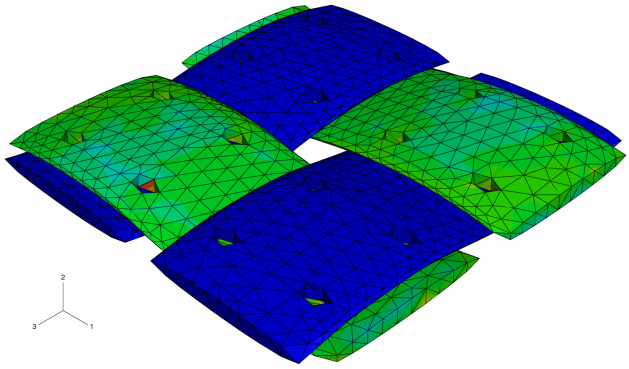

Figure 35 One Unit Cell with 1% d= 0.2794 mm (0.011 in) Z-pin

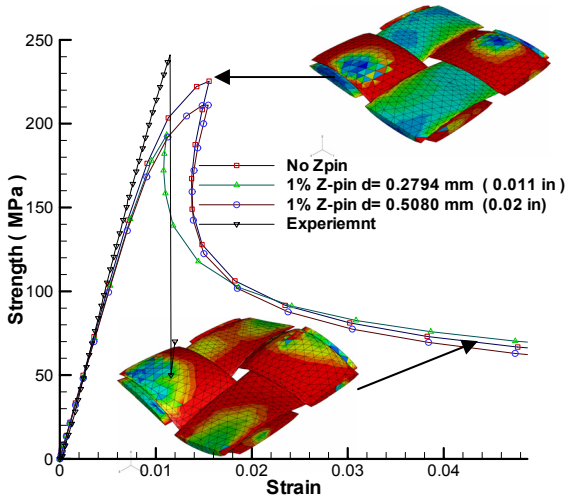

Figure 36 Comparison of Simulations with Experimental Results